Modification of the microstructure by rotating magnetic field during the solidification of Al-7 wt.% Si alloy under microgravity

Yuze Li, Nathalie Mangelinck-Noël, G Zimmermanm, L. Sturz, Henri Nguyen-Thi

Modification of the microstructure by rotating magnetic field during the solidification of Al-7 wt.% Si alloy under microgravity

*Y. Z. Li [(a)], N. Mangelinck-Noël [(a), *], G. Zimmermann [(b)], L. Sturz [(b)], H. Nguyen-Thi [(a)]*

[(a)] Aix Marseille Univ, Université de Toulon, CNRS, IM2NP, 13397 Marseille, France

[(b)] ACCESS e.V., Intzestraße 5, 52072 Aachen, Germany

Abstract

Directional solidifications of Al-7 wt.% Si alloy were carried out under microgravity on board the International Space Station to investigate the impact of a rotating magnetic field (RMF) on the solidified microstructure. It has been found that the RMF significantly influences the solidified microstructure in the conditions corresponding to the lowest growth rate, whereas it has negligible influence on the microstructure under the highest growth rate, indicating that the RMF intensity and the forced liquid flow are too weak, compared to the solidification front velocity, to impact the microstructure. For the lowest growth rate applied, the RMF application results in a more uniform eutectic phase distribution and a smaller dendrite arm spacing. This is ascribed to the RMF induced forced liquid flow that makes more uniform Si concentration in the bulk liquid above the solid-liquid interface. Additionally, the RMF application possibly modifies the columnar dendritic network by changing dendrite growth directions. This observation can be attributed to the combined effect of the RMF induced forced liquid flow and of the thermoelectric magnetic force on the dendrites resulting from the application of the RMF as well.

Keywords: Aluminum alloy; Directional solidification; Microstructure, Dendrite growth; Microgravity; Rotating magnetic field

1. Introduction

The final properties of the industrial casting products depend significantly on the solidification microstructure, which is the first step of most manufactured metallurgical products [1]. During the solidification of a binary hypoeutectic alloys, the final microstructure consists of a dendritic network surrounded by the eutectic phase. The features of the dendritic structure (columnar or equiaxed), the average spacing and the eutectic (percentage and distribution) strongly affect the material properties, and are related tightly with the alloy defects [2]. Therefore, the deep understanding of the formation of the solidified dendritic and eutectic structures, as well as of the relationship of the solidification microstructure characteristics with the solidification conditions, are mandatory to master the industrial processes more precisely and to be able to verify the predictability of simulation tools.

It is well established that the liquid flow during the solidification process significantly influences the formation and evolution of the solidified microstructure, because of the flow induced modifications of the thermal and solute distributions [3-6]. Thus, the possible use of forced flow has drawn widespread attentions in terms of material physics for many decades. Particularly, the application of a magnetic field (MF) was found to be an effective way to investigate the flow effect and to improve the solidified microstructure by controlling the liquid flow [7-10]. Recently, several effects of MF application were reported, such as refining the dendrite grain structure [11], alleviating or inducing the macrosegregation by the redistribution of the solute in the liquid [12-14], reducing the natural convection effect by impeding the liquid flow under gravity condition [15], and triggering the columnar to equiaxed transition (CET) of the dendritic structure [16, 17]. Moreover, the thermoelectric magnetic force (TEMF) is a Lorentz force, particularly important in solidification. It is due to the interaction of the applied magnetic field with the thermoelectric (TE) currents, generated along any non-isothermal solid-liquid interface by the differences of the solid and liquid Seebeck coefficients, in the same way

as the thermocouple principle [12, 18]. During the solidification, the TEMF acts not only on the liquid, inducing the thermoelectric magnetic convection (TEMC) in the liquid phase [19, 20], but also on the movement of the dendrites, fragments or grains [16, 21, 22].

The rotating magnetic field (RMF) has already been widely used in the metallurgical industry to modify the microstructure during the solidification [23-25]. To date, there have been some studies, both via experimental and simulated methods, focusing on this aspect [26-30]. The characteristic of a RMF is controlled by two main parameters: the angular frequency f and the intensity B [24, 26]. In general, the sample main axis (solidification direction) and the rotation axis of the RMF are aligned. The rotation of the magnetic field with the frequency f drives an azimuthal liquid flow around the sample main axis known as the primary flow, which induces a flow parallel to the sample main axis known as the secondary flow [24, 26, 29, 31]. The liquid flows exist not only in the liquid ahead of the solidification front, but also in the interdendritic region in the mushy zone. Thus, both thermal and solute fields can be significantly modified and consequently the solidified microstructure. The RMF driven flow can homogenize the solute distribution and suppress the shrinkage flow and take over the natural convection [26], but may also result in axial macrosegregation, as reported in the directional solidification of AlSi7Mg0.6 alloy under RMF [24, 32]. Furthermore, the entire complex dendritic network, with an array of primary, secondary and some higher order arms, can be significantly modified. For instance, the primary arm spacing λ_1 significantly decreases, whereas the secondary arm spacing λ_2 increases during the solidification of the A357 alloy under the action of RMF, as reported by Steinbach and Ratke [33]. Finally, the RMF by its action on dendrite fragments and new nucleated grains can trigger or improve the CET [8, 24, 32, 34, 35].

However, the detailed mechanisms of the RMF effect are not completely clarified quantitatively, with a lot of key issues that still need to be figured out in more details. Particularly, the natural convection and other gravity inducing phenomena would make it more

complex to analyze the RMF effect mechanism, since they induce the variations of both the thermal/solute field and the movement of the grain at the same time as the magnetic field [4, 36, 37]. Although the RMF effects can be simulated without consideration of the gravity effects [26, 38], the verification of these simulations and detailed quantitative comparison with the experiments are still hard due to the lack of benchmark experimental results.

Solidification under microgravity (μg) is a method of choice to answer to these questions. It can effectively suppress the gravity effects on heat/solute transportation, grain movement and others [2, 39, 40], which allows to deepen the study of the magnetic field effect mechanism only. The Material Science Laboratory (MSL) on board the International Space Station (ISS) is made available by the European Space Agency (ESA) to provide a platform to investigate the major scientific issues in solidification. Within the ESA project CETSOL (Columnar to Equiaxed Transition in SOLidification processes) [41, 42], directional solidification experiments of Al-7 wt.% Si alloy were carried out with or without RMF in the MSL. In this paper, by comparing the cases with or without RMF, the influence of the RMF on both the thermal conditions and the microstructure have been specifically investigated including the solute distribution, the dendrite growth and the CET.

2. Experimental

2.1. Experiment details

Microgravity solidification experiments (μg) with or without rotating magnetic field (RMF) were conducted under low and high furnace pulling velocities using the MSL Bridgman-type Solidification and Quenching Furnace (SQF), which was described in details in our previous studies [43]. The SQF furnace, which consists of hot and cold zones separated by an adiabatic zone, and the sample cartridge assembly (SCA) are schematized in Fig.1. The cold zone is realized by a Liquid Metal Ring (LMR) and the hot zone is equipped with four heaters H1-H4

that can be adjusted independently to achieve the required temperature gradient along the sample main axis. Solidification of the alloy is performed by the controlled displacement of the furnace relatively to the fixed SCA at a chosen velocity, which can be varied during the experiment. The metallic alloy sample (a cylindrical shape with 8 mm in diameter and 245 mm in length) is mounted inside an Al_2O_3 tube crucible together with Shapal plugs at both ends. Twelve thermocouples (TC1-TC12), spaced by 20 mm, are located in four machined external grooves at the outer surface of the crucible to record the temperature profile (purple dots in Fig.1).

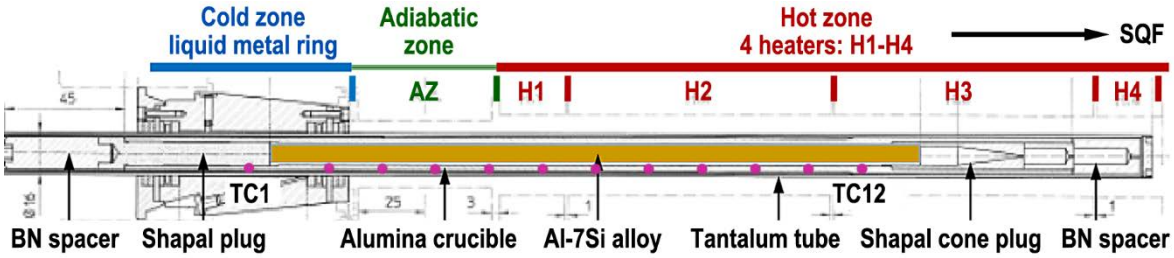

Fig.1. Sketch of the SQF furnace and SCA cartridge for a CETSOL Batch 2a experiment before solidification with the integrated Al-7Si alloy sample.

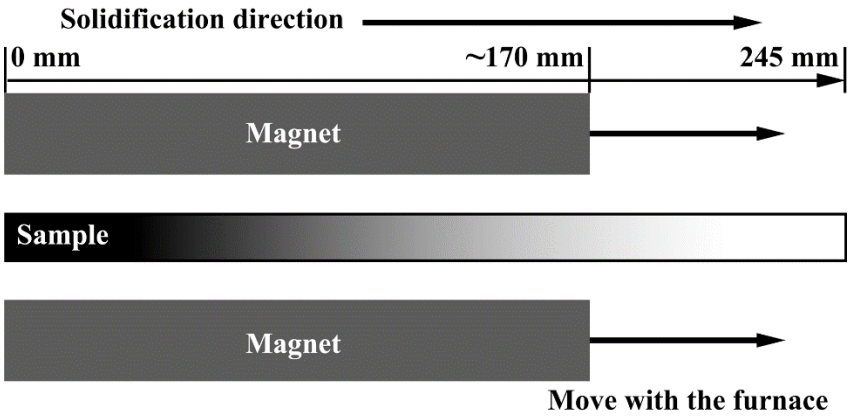

Fig.2. Sketch of rotating magnetic field magnet integrated into the SQF furnace at the start position of solidification.

The RMF generating device is integrated into the SQF furnace outside the heating elements and the liquid metal cooling ring (Fig.2). The length of the magnet, giving the range of the generated RMF, is about 170 mm. The lower end of the magnet is close to the lower end of the sample (0 mm reference position along the sample main axis) as shown in Fig.2. A moderate RMF is applied in this study with a frequency f = 57 Hz and a relatively small magnetic field strength of B = 0.5 mT, to avoid the RMF induced macrosegregation as reported in previous studies [44]. The solid/liquid interface is situated approximately at the central position of the magnet assembly during the solidification to ensure the efficiency of the RMF.

Grain refined Al-7 wt.% Si alloy (Al-7Si+GR in table 1) and non-grain refined Al-7 wt.% Si alloy (Al-7Si in table 1) provided by Hydro Aluminum Rolled Products GmbH are used in this work. 0.5 wt% of master alloy AlTi5B was added for the grain refinement.

Table 1. Control parameters: v_n is the furnace pulling rate and z_n the solidification length under v_n for stage n. GR indicates grain refinement of the alloy. The RMF column indicates whether the RMF (f = 57 Hz, B = 0.5 mT) was applied or not.

Sample	Alloy	RMF	Initial	Stage I		Stage II			Stage III
			G, K/mm	v_1, mm/s	z_1, mm	v_2, mm/s	z_2, mm	R, K/s	
B2F1	Al-7Si+GR	No	4	0.02	20	0.2	50	0.13	Quenching
B2F2	Al-7Si	Yes	4	0.02	20	0.2	50	0.13	Quenching
B2F5	Al-7Si+GR	No	4	0.02	30	0.02	50	0.13	Quenching
B2F6	Al-7Si	Yes	4	0.02	30	0.02	50	0.13	Quenching

The designated samples presented in this work and the corresponding solidification parameters are summarized in Table 1. The solidification procedure consists of three successive stages:

- Stage I: For all experiments, the objective of the Stage I is to achieve a steady-state columnar growth, with no RMF. Accordingly, the initial temperature gradient (G) is about 4 K/mm and the solidification is initiated by the slow pulling rate of the furnace at v_1 = 0.02 mm/s. No RMF is present during stage I in all cases.

- Stage II: To provoke the columnar-to-Equiaxed Transition, two different second stages are defined : *(i)* For B2F1 and B2F2, the Stage II is triggered by a simultaneous sudden pulling rate jump from v_1 = 0.02 mm/s to v_2 = 0.2 mm/s and a cooling down of the hot zone at R = 0.133 K/s. *(ii)* For B2F5 and B2F6, the pulling rate is not modified ($v_1 = v_2$ = 0.2 mm/s) and the hot zone is cooled down at R = 0.133 K/s. Thus, a decrease of the temperature gradient G is induced in stage II in the four experiments. The displacement length is 50 mm in stage II for all samples. Additionally, for B2F2 and B2F6, the RMF is turned on during the whole duration of stage II to induce a forced melt flow in these two samples. The comparative study of experiments with (B2F2/B2F6) and without (B2F1/B2F5) RMF allows analysing the effect of RMF upon the solidification microstructure.

- Stage III: The quenching of the sample induced by a fast furnace pulling is applied to complete the solidification. During this final stage, the RMF is turned off again for all experiments, the temperature gradient and cooling rates are no longer controlled, but the temperature profiles are still recorded.

2.2. Microstructure characterization

The characterization methods in the present study have been described in detail in our previous study [43]. After their return to Earth, samples are cut into transverse and longitudinal sections of 30 mm in lengths and prepared for metallographic analysis. The sketch of the cutting scheme, which is the same for all samples is shown in Fig.3 for the processed sample B2F1. Then, longitudinal sections cut close to the centerline are mechanically polished with diamond suspension to reveal the dendrite structures by optical microscopy (OM). Finally, electrolytic

etching is performed to distinguish dendrites with different crystallographic orientations in different colors using an optical polarized light microscope (OM) and thereby to reveal the grain structure.

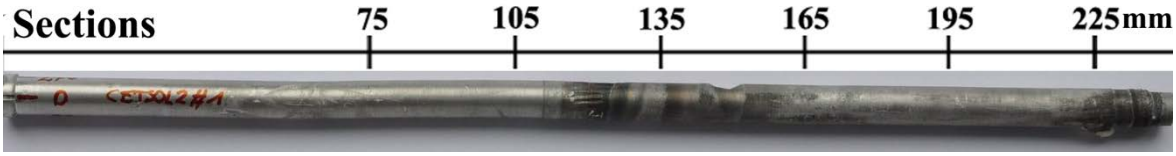

Fig.3. Optical image of the processed sample B2F1 with the identification of the cross-section positions.

The optical microscopy images of longitudinal sections were used to measure the eutectic percentage (E%) and the dendrite arm spacing (DAS). The images are segmented into binary images to distinguish the dendrite phase (white) from the eutectic (black). Based on the binary images, the E% maps and the E% profiles along the main cylindrical sample axis are determined using a box-averaging method. The DAS is measured using a linear-intercept method [43]. For one data point of DAS, 1000 lines are generated in random orientation. The box size used to calculate the E% in the maps is 0.5 mm along the direction of the sample central line axis, and 0.4 mm in width.

The box size used to calculate both E% and DAS profiles is 0.5 mm in length and equal to the sample diameter in width. It is worth to mention that the measured DAS is not equal to the primary or secondary dendrite arm spacing but is a measurement of the average characteristic scale of the dendritic network [2, 45].

3. Results

3.1. Analysis of the processing parameters

The recorded cooling curves for all samples are shown in Fig.4, with identification of the successive stages delimited by the starting times of the furnace movement. From Fig.4, it can

be seen that the thermal histories recorded are very similar for B2F1 and B2F2, and for B2F5 and B2F6, indicating that the influence of the grain refiner (GR) and of the rotating magnetic field (RMF) in stage II are negligible as concerns the recorded temperatures. This conclusion is in agreement with previous experiments [43].

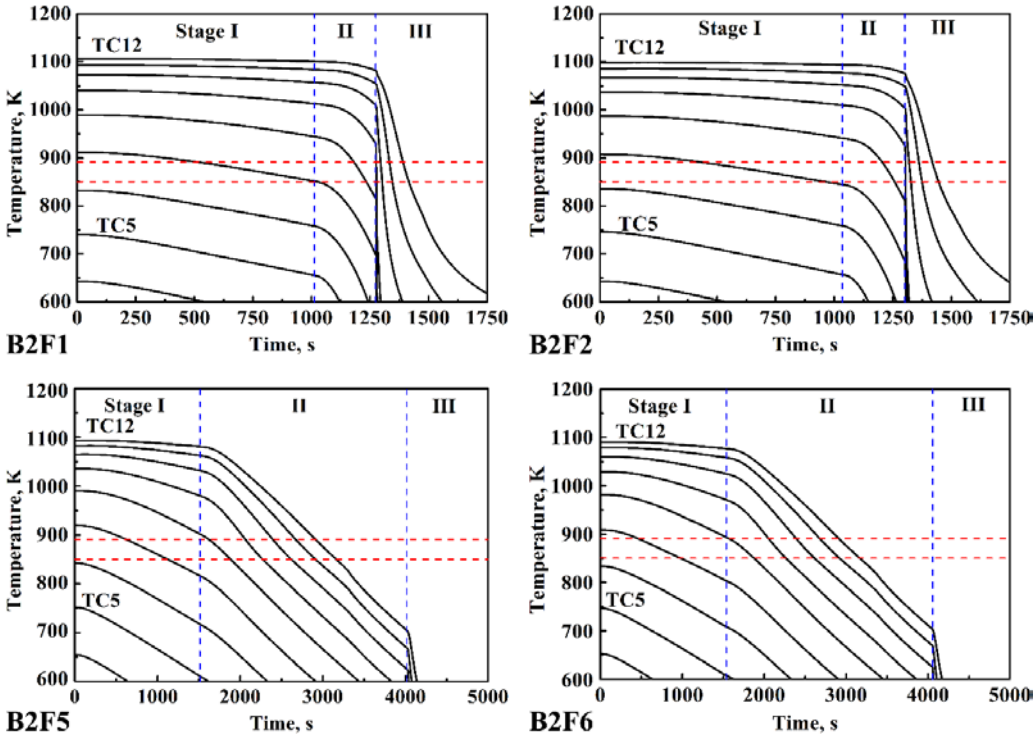

Fig.4. Temperature curves recorded during the experiments. Liquidus and eutectic isotherm positions (T_L=891 K and T_E=850 K) are indicated with red horizontal dashed lines. The limits between the different solidification stages are indicated with blue vertical dashed lines.

Fig.5 shows the actual growth conditions of all the samples, namely the temperature gradient ahead of the liquidus isotherm (T_L = 891 K for Al-7wt%Si) G_L (Fig.5a) and the velocity of the liquidus isotherm v_L (Fig.5b), which are calculated based on the temperature profiles with the procedure described in our previous work [43]. The values of G_L and v_L are calculated every 10 mm as shown in Fig.5. Additionally, the transition positions between the successive stages (blue dashed lines in Fig.5) are also obtained from the temperature profiles as explained in detail in our previous work [2]. The average values of the G_L and v_L for each stage are calculated

and gathered in Table 2. The transition positions between stages II and III for B2F5 and B2F6 cannot be determined because the temperatures at the level of the highest thermocouple TC12 (position: 182.5 mm) at the time of transition from stage II to III are much lower than the liquidus temperature (891 K) as shown in Fig.4. Thus, only the initial parts of about 25 mm in stage II, are considered when calculating the average values of G_L and v_L, corresponding to the microstructure shown later in Fig.6.

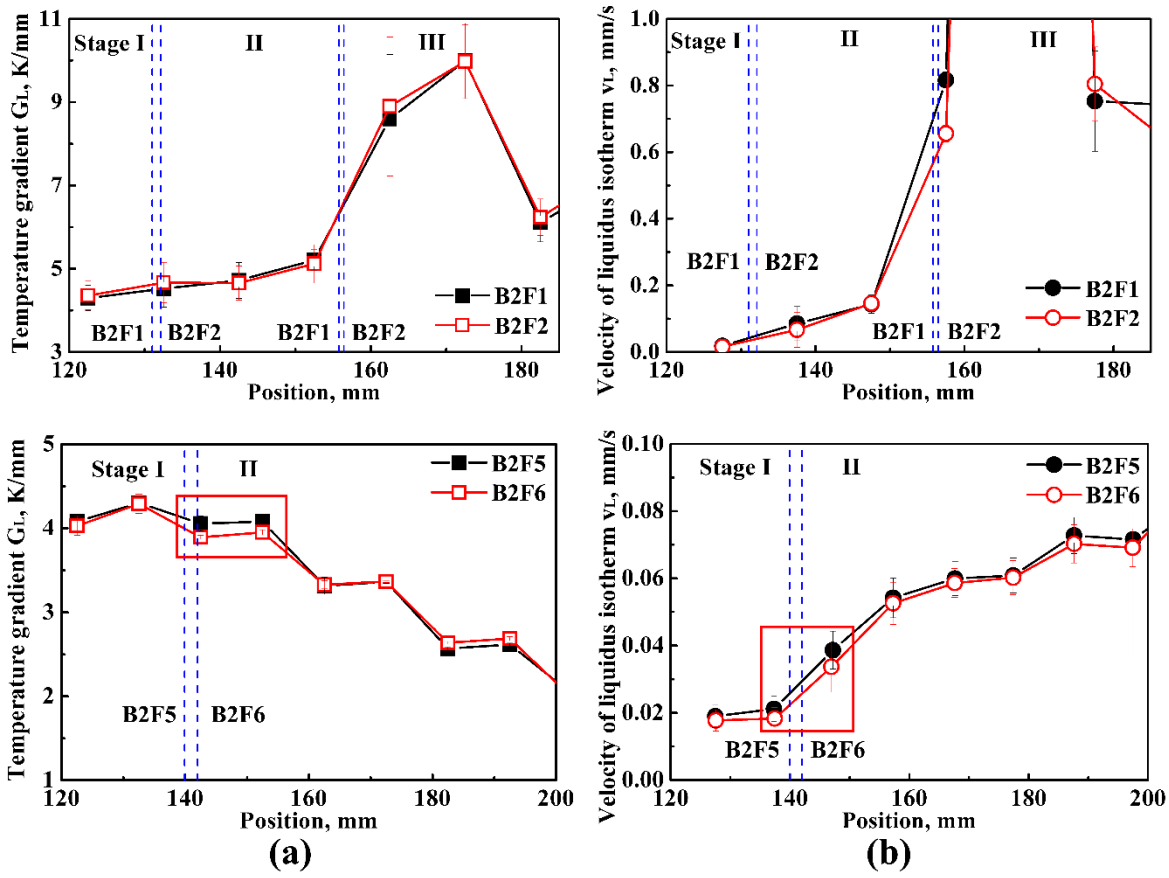

Fig.5. (a) Calculated temperature gradient ahead of the liquidus isotherm (G_L) and (b) calculated average velocity of the liquidus isotherm (v_L) during the solidification. The limits between the different solidification stages for the corresponding samples are indicated with blue vertical dashed lines.

The temperature gradient (Fig.5a) and the liquidus velocity curves (Fig.5b) for both B2F1 and B2F2 almost overlap each other, indicating that the growth conditions of B2F1 and B2F2 are comparable during the whole experiment and confirming the negligible influence of the GR and RMF on the thermal conditions during the solidification at high furnace puling velocity. For B2F1 and B2F2, the temperature gradient and the growth velocity both increase due to the change of the solidification conditions (mainly the increase of the furnace pulling rate) from stage I to stage II as shown in Fig.5(a, b) and in Table 2. From stage II to stage III, both the growth velocity and the temperature gradient sharply increase as shown in Fig.5a and b due to the quenching of the samples.

Table 2. Calculated average values of the temperature gradient G_L, velocity v_L of the liquidus isotherm, eutectic percentage (E%) and dendrite arm spacing (DAS) in stages I and II.

Sample	Stage	G_L, K/mm	v_L, mm/s	E, %	DAS, µm
B2F1	I	4.4	0.02	57	55
	II	4.8	0.11	46	33
B2F2 (RMF)	I	4.5	0.02	55	57
	II	4.8	0.11	48	35
B2F5	I	4.3	0.020	46	70
	Initial part of II	4.0	0.043	43	63
B2F6 (RMF)	I	4.4	0.018	45	60
	Initial part of II	3.9	0.041	39	58

The growth conditions of B2F5 and B2F6 exhibit slight differences around the position of 140 mm as highlighted by the red rectangles in Fig.5c and 5d. The values of both G_L and v_L are slightly lower in B2F6 (with RMF) than in B2F5 at this level, suggesting that the growth conditions might be slightly influenced by the RMF during the solidification at low furnace pulling rate ($v_1 = v_2 = 0.02$ mm/s). This effect of the RMF on the G_L and v_L in B2F6 will be discussed later in Section 4.2. Second, the global evolution tendencies of both G_L and v_L are identical for B2F5 and B2F6: the calculated G_L gradually decreases whereas the calculated v_L gradually increases in stage II, which is due to the cooling down applied only to the hot zone in this stage (Table 2).

Finally, according to the temperature gradient, the length of the mushy zone during the solidification process (L_{MZ}, distance between the liquidus and eutectic isotherms) can also be estimated to a value of about 10 mm in stage I and II for all samples.

3.2. Analysis of the microstructure

Fig.6a1 to 6d1 shows the microstructures of the four samples obtained by color etching along the longitudinal sections. The blank regions correspond to the material loss between two sections due to the preparation of cross-sections. The furnace pulling velocities at different solidification stages, with the range given in Fig.5, are indicated at the left side of the section images. As shown in Fig.6a1 to 6d1, columnar structure is observed from the initial region to the entire stage I for all samples as expected under these growth conditions [43, 46]. Interestingly, from stage I to stage II, different microstructure transition occurred in the different samples. For B2F1 (Fig.6a1), finer dendrites are observed in stage II compared to stage I and a columnar to equiaxed transition (CET) is observed (CET start position is indicated in Fig.6a1 by the red dashed line). For B2F2 (Fig.6b1), the dendritic microstructure gets much finer in stage II, just as for B2F1, but without CET. The corresponding DAS measurements (Table 2) confirm quantitatively the fact that a finer microstructure is observed in stage II. For

B2F5 and B2F6 (Fig.6c1 and 6d1), the dendrite microstructures do not significantly change from stage I to stage II: similar coarse columnar dendrites are obtained. This is directly related to the fact that the same furnace pulling rate is applied in both stages I and II (v_1=v_2=0.02 mm/s) and indicates that the applied slow decrease of the temperature gradient has negligible influence on the solidified microstructure.

Fig.6a2 to 6d2 show the corresponding eutectic percentage (E%) maps along the longitudinal sections. The eutectic is formed in the interdendritic regions following the dendrite growth because of the accumulation of solute rejected by the dendrites. As shown in Fig.6a2 to 6d2, large eutectic pockets, evidenced by almost black regions, and inhomogeneous eutectic distribution are observed in stage I for all samples, which is directly related to the coarse columnar structure. For B2F1 and B2F2 (Fig.6a2 and b2), with a higher pulling rate in stage II, the eutectic feature is comparable: much more uniform distribution with much lower average E% even though the microstructure is different. For B2F5 and B2F6 (Fig.6c1 and d1), the eutectic features changed slightly from stage I to stage II with obvious difference between both samples. For B2F5 (Fig.6c2), some large eutectic pockets and non-uniform eutectic distribution can still be observed whereas for B2F6 (Fig.6d2), the eutectic distribution is more uniform, with no large eutectic pockets.

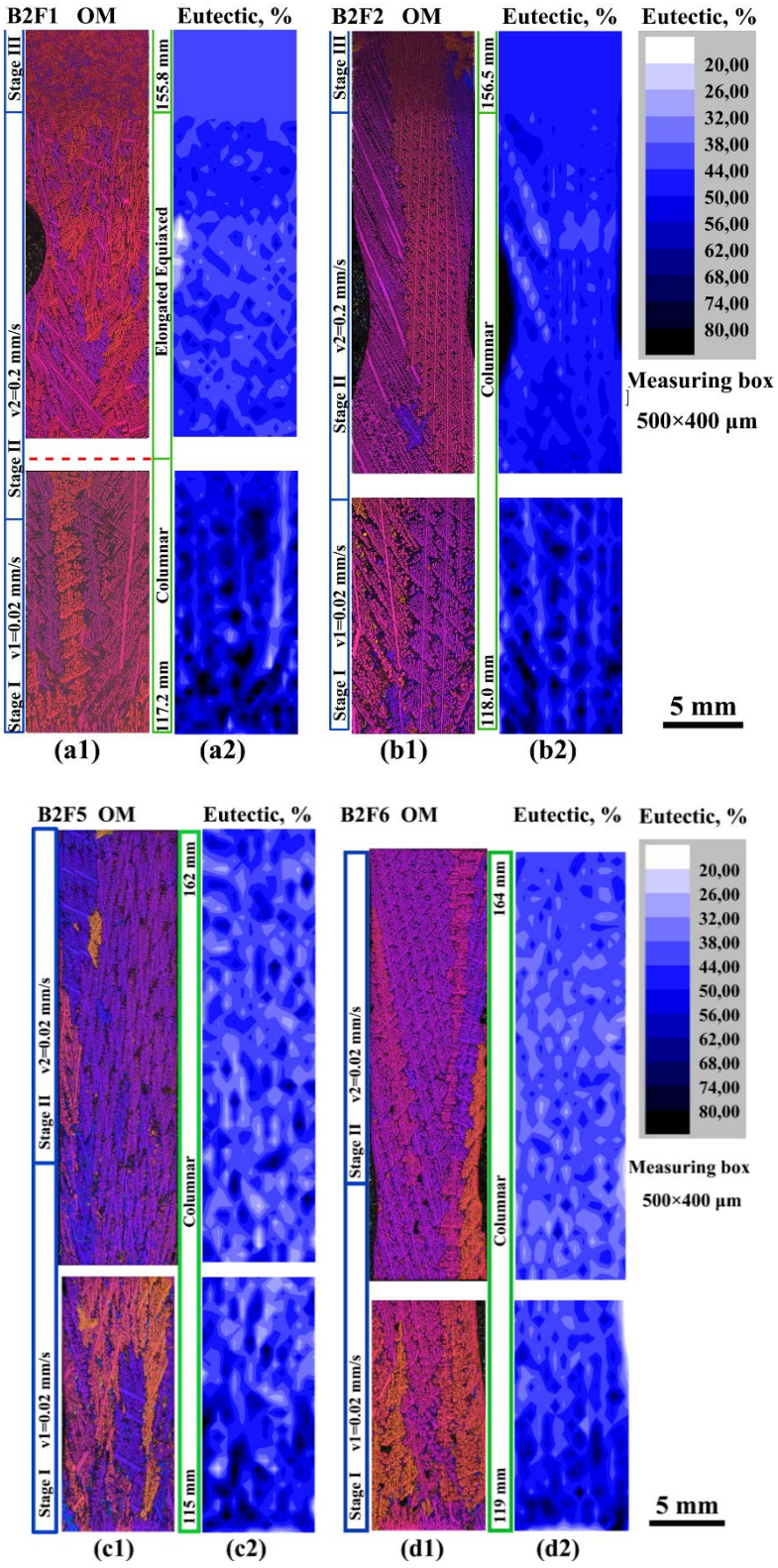

Fig.6. Microstructure revealed by color etching along longitudinal sections (a1, b1, c1, d1) and corresponding eutectic percentage distribution maps (a2, b2, c2, d2) for all samples. The red dashed line in (a1) gives the highest position of the columnar grains issued from the initial dendritic zone.

For the quantitative analyses of the microstructure evolution, the E% and dendrite arm spacing (DAS) profiles along the solidification direction have been calculated as described above and are presented in Fig.7. The evolution of E% and DAS in B2F1 and B2F2 are nearly the same, evidenced by equivalent average values in each stage as shown in Table 2. When comparing B2F5 and B2F6, during Stage I the average E% decreases from the initial solidification region and then remains nearly constant. However, slight increase of the average E% and DAS are observed around the transition position from stage I to stage II in B2F5, whereas in B2F6 the E% and DAS remain almost constant in this region, as shown by the black rectangles in Fig.7. Additionally, the average values of E% and DAS in stage II and the average DAS in stage I are lower in B2F6 compared to B2F5 as shown in Table 2.

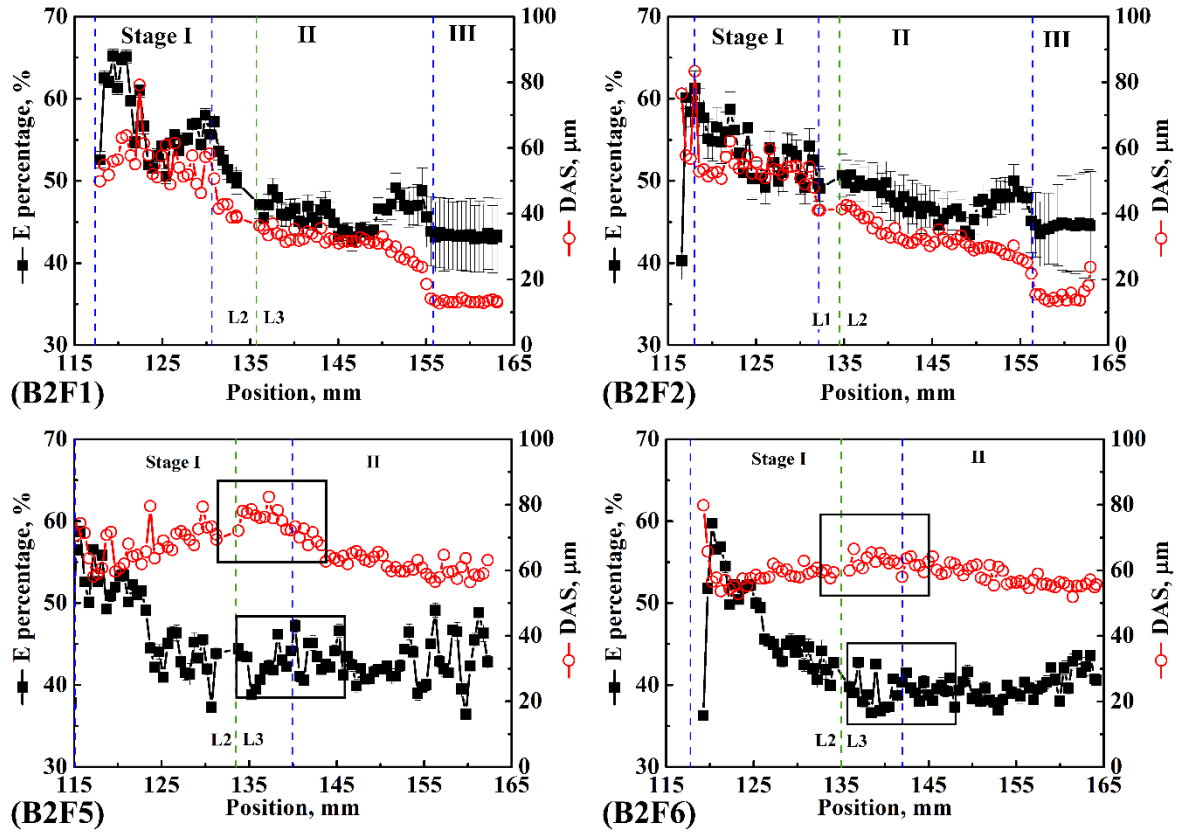

Fig.7. Mean eutectic percentage and mean DAS vs. position along the central line in the longitudinal direction of the samples. The blue dashed lines show the stage transition positions and the green dashed lines show the section cutting positions.

3.3. Deflected dendrite growth in B2F6

Fig.8 shows the dendrite growth around the transition position from solidification stage I to stage II of both B2F5 and B2F6 (part of the longitudinal sections from Fig.6c1 and 6d1), at the lower furnace pulling rate (v_1=v_2=0.02 mm/s). As shown by the label at the top of Fig.8b, corresponding to the microstructure of B2F6, the RMF was turned on just at this position during the solidification experiment. As displayed in B2F5, dendrites originating from stage I (dendrites 1, 2 and 3 in Fig.8a) simply continue to grow along their original directions as shown by the white arrows in Fig.8a. This type of continuous dendrites originating from stage I is also observed in B2F6, as shown in Fig.8b (dendrites 1, 2 and 3). However, in B2F6, the growth of these dendrites is deflected in stage II, as shown by the green arrows in Fig.8b. The position where the dendrite growth direction changes is close to the transition position from stages I to II, which is also the position at which the RMF was turned on during the solidification. After this particular position, the dendrite growth continues in stage II in the same direction without any subsequent deflections (Fig.8b).

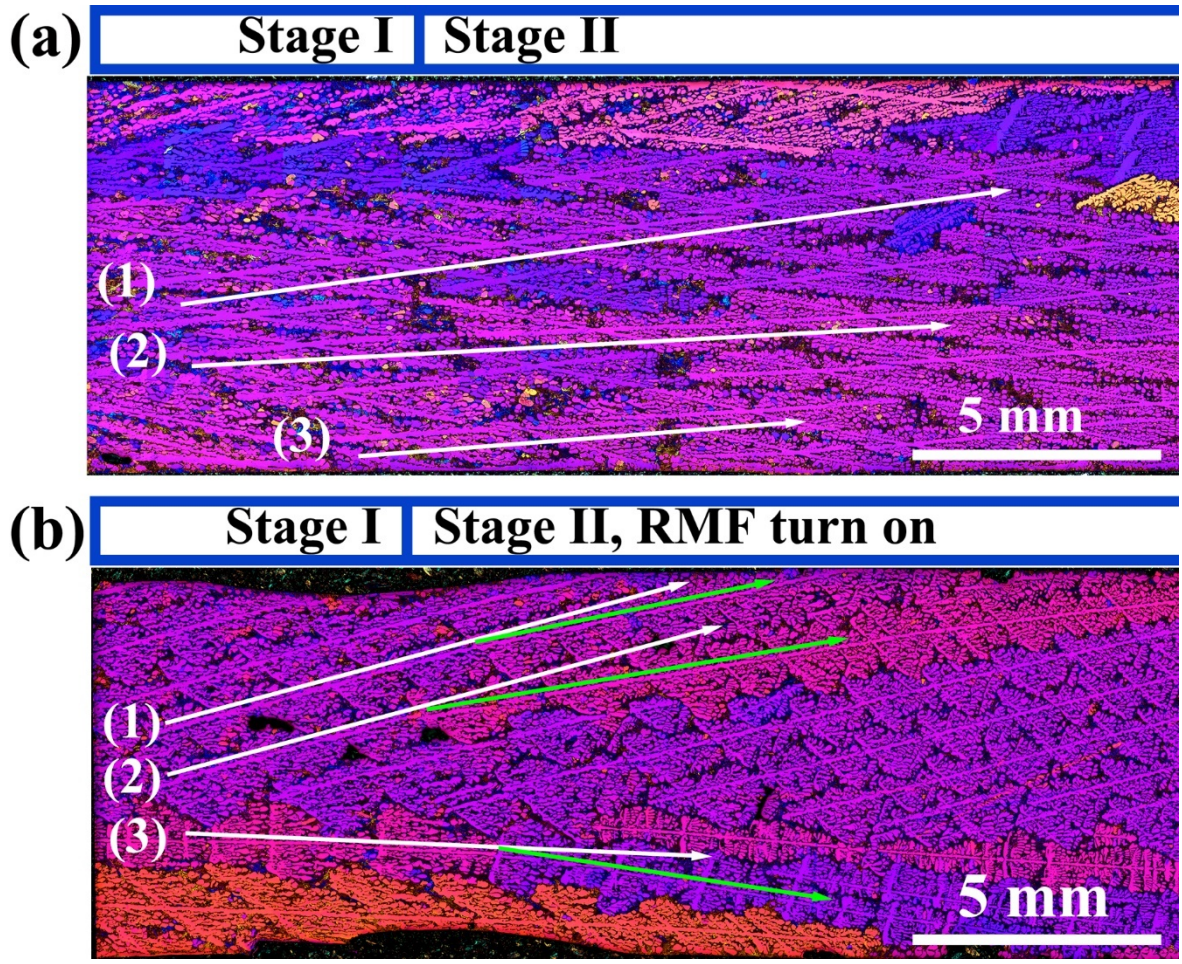

Fig.8. Dendrite growth with or without the application of RMF in the regions around the transition position from stage I to stage II at the lower furnace pulling rate (v_1=v_2=0.02 mm/s): (a) B2F5 without RMF, (b) B2F6 with RMF applied in stage II. The white arrows in (a) and (b) show the initial growth direction of the dendrites. The green arrows show the new direction after the RMF is turned on.

4. Discussion

4.1. Effects of the solidification parameters (G, v, R…) on the microstructure

The microstructure evolution and the relationship with the solidification parameters in B2F1 and B2F2 have already been discussed in detail in our previous work [43]. The finer structure in stage II compared with that in stage I for both B2F1 and B2F2 and the occurrence of CET in stage II of B2F1 is due to a combination of a higher growth rate and lower temperature gradient.

For the microstructure evolution in B2F5 and B2F6, first, the more uniform eutectic distribution in stage II, and the decrease of both E% and DAS from stage I to stage II of both samples (Table 2 and Fig.7), are the consequences of the cooling down of the heat zone in stage II. The decreasing temperature of the heat zone results in a decrease of G_L and an increase of the dendrite growth velocity, as indicated by the liquidus isotherm velocity (v_L, Table 2 and Fig.5). Therefore, more homogeneous eutectic distribution and lower E% are obtained, accompanied with the decrease of the microstructure size (DAS), due to the stronger dendritic branching triggered by the higher dendrite tip velocity in stage II of B2F5 and B2F6 [2, 46]. As expected, CET took place in B2F1 because of the presence of grain refiners combined with an increase of the growth rate. On the contrary, no CET is observed in the other grain refined experiment (B2F5), due to the fact that no increase of the growth rate is applied [43].

CET is not observed in both non-refined samples (B2F2 and B2F6) even though a RMF is applied. Indeed, the RMF is expected to trigger CET by transporting some fragments to the columnar front. However, there are two main reasons for the absence of CET: 1. The RMF may be not sufficiently strong to provoke massive nucleation or transport of equiaxed grains ahead of the columnar dendritic front; 2. The new nucleated grains ahead of the columnar dendritic front could be transported into the bulk liquid far away.

4.2. Effect of the RMF on the thermal condition and on the microstructure

The thermal condition differences (Fig.5 and Table 2) and the microstructure differences (Fig.6, 7, 8 and Table 2) between B2F5 and B2F6 are mainly attributed to the application of the RMF in B2F6, which was turned on at the time of the transition from solidification stage I to stage II. The RMF device translates with the same velocity as the furnace, which is constant at 0.02 mm/s in both stages I and II, while the liquidus isotherm velocity increases in stage II (Figure 5). The strongest influence of the RMF occurs around the transition position from stage I to II,

and generally decreases in the following solidification process as can be seen from the thermal condition and microstructure differences shown in Fig.5 to 8 and Table 2.

As mentioned in the introduction, the applied RMF can have two main impacts on solidification: a forced liquid flow and a thermoelectric magnetic force acting on the dendrites [14, 22, 24, 47, 48].

4.2.1. Estimation of the RMF induced melt flow

From the simulations of a RMF with a moderate intensity of only B=0.5 mT and f=57 Hz performed earlier within the CETSOL project [44], the detailed and quantitative patterns of the forced liquid flow due to the RMF can be estimated. The simulations were performed using the process parameters and the experimental setup of the flight experiments, but assuming a flat solid-liquid interface. Main characteristic of the simulated flow pattern are (i) an axial flow which can create axial transport of heat and solute in the melt, and (ii) an azimuthal flow, which supports homogenization of the melt ahead of the solid-liquid interface.

According to the simulation results [44], the maximum value of the forced liquid flow velocity in azimuthal direction is about 0.2 mm/s, whereas the maximum velocity along the sample axis direction is only 0.003 mm/s in the center region of the sample. The liquid flows due to the RMF, co-exist in front of the dendrite tip and in the deep interdendritic regions. From the simulations [24, 31], the main liquid flows patterns can be schematized by the black dash lines in Fig.9. The liquidus (T_L) and the eutectic (T_E) isotherms are indicated by the blue horizontal dashed lines. The solute in interdendritic regions is schematized by the gray color in Fig.9, with higher gray scale indicating higher solute concentration. Under the microgravity condition (µg) in this experiment, the forced flow due to the RMF only superimposes with the shrinkage flow in the sample. Consequently, the RMF forced flow affects the thermal and solutal distribution in the liquid both in front of the dendrite tip and in the deep interdendritic regions during the solidification.

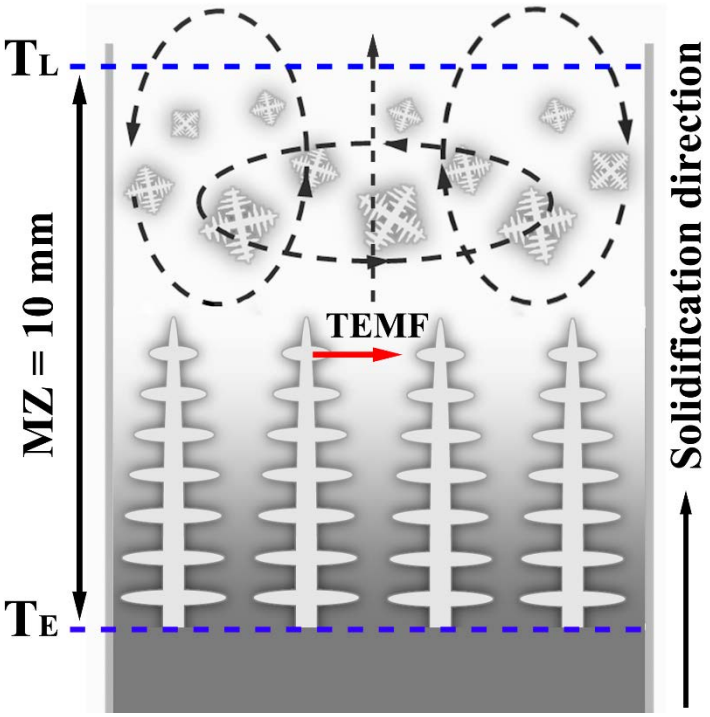

Fig.9. The black dashed lines and circles show the schematic patterns of the liquid flow due to RMF during solidification. T_L and the upper blue dashed line, and T_E and the bottom blue dashed line indicate the liquidus and the eutectic isotherm positions, respectively. The red arrow shows the representative direction of the TEMF.

4.2.2. RMF effect relatively to the furnace pulling rate

As described in Sections 3.1 to 3.2, no effect of the RMF can be evidenced for the highest furnace pulling rate in sample B2F2. The RMF has negligible influence on both the thermal conditions (G_L and v_L) and the microstructure (E% and DAS, as well as the dendrite growth direction). This could be attributed to the moderate intensity of the RMF, which is only B=0.5 mT. Indeed, when compared with the pulling rate in stage II of B2F2, the forced liquid flow intensity due to the RMF in B2F2 is smaller both in the deep mushy zone and ahead of the large dendrites. Correspondingly, this moderate RMF is neither sufficient to result in any thermal difference nor to trigger any significant microstructure difference in B2F2.

Besides, an effect of the RMF is observed for the lowest furnace pulling rate (sample B2F6), where especially the azimuthal flow velocity is significantly higher than the solidification velocity. During the solidification process in µg, the temperature and the solute gradients co-exist in the liquid along the solidification direction: the temperature generally increases and the solute (Si) concentration generally decreases from the bottom to the top of the sample as shown in Fig.9. Due to the liquid flows, hot liquid in the top region flows toward the bottom part in the sample edge regions, which consequently increases the temperature of the sample bottom, together with the decrease of the temperature in the sample top due to the liquid flow in the sample centerline region. Therefore, the consequence is a temperature homogenization and thus, a temperature gradient decrease (slightly lower in B2F6 compared to B2F5). The slight decrease of the detected liquidus isotherm velocity as shown in Fig.5b is mostly ascribed to the increasing temperature of the solidification front due to the liquid flow in the sample edge regions.

Additionally, according to the simulation results [44], due to forced azimuthal liquid flow, a more uniform Si distribution is achieved in the liquid when the RMF (B=0.5 mT, f = 57 Hz) is applied in these experiments. The Si concentration in the interdendritic region in B2F6 under RMF is even close to 7 wt.%, which is the Si concentration of the liquid far from the solidification front. Therefore, large eutectic pockets which can develop without RMF in B2F5 as shown in Fig.6c2, are not observed in B2F6 (Fig.6d2). Consequently, more uniform eutectic distribution and lower E% are obtained in B2F6.

Additionally, the much more constant DAS around the transition position from stage I to II as shown in Fig.7, as well as the average DAS decrease shown in Table 2, could also be attributed to the RMF forced liquid flow. Generally, the application of the RMF was proven to reduce the primary dendrite spacing due to the forced liquid flow and the modification of the solute distribution in the interdendritic region [9, 27]. As mentioned above, the measured DAS is not

equal to the primary dendrite spacing but is an average measurement which takes also into account the secondary, tertiary and other higher-order dendrite arm spacing. Thus, the decrease of the primary dendrite spacing due to the RMF contributes to the decrease of DAS in B2F6 experiment.

4.2.3. Thermoelectric magnetic force on the dendrites

Apart from the forced liquid flow, the thermoelectric magnetic force (TEMF) also acts on the dendrites during the solidification submitted to a magnetic field [47]. The temperature gradient along the solid-liquid interface generates a TE current in the close vicinity of the columnar dendrites [49]. Therefore, a Lorentz force (i.e. the TEMF) is imposed on the dendrite when applying a magnetic field, due to the interaction between the magnetic field and the TE current. In the study by Wang *et al.* [50, 51], the direction of the TEMF was perpendicular to the solidification direction when the magnetic field was applied perpendicularly to the solidification direction. For the RMF applied in the present work, the direction of the magnetic field vector is perpendicular to the solidification direction, but with a rotation around the centerline of the rod sample. Therefore, a TEMF perpendicular to the solidification direction, i.e. nearly perpendicular to the dendrite growth direction as shown in Fig.9 (red arrow), is expected with the same rotation around the sample centerline as the applied magnetic field applied. Consequently, the continuous growth direction of the columnar dendrites in stage II can be deflected from their original direction originating from stage I as seen in B2F6 (Fig.8), due to the action of the TEMF. However, because of the varied and complicated B direction with the application of a RMF, some more detailed simulations would be useful to study more accurately the effect of the TEMF on the dendrite growth as performed for example in the case of a static magnetic field in previous work [50].

5. Conclusion

Microgravity (μg) solidification experiments of Al -7 wt.% Si alloy have been carried out with or without rotating magnetic field (RMF). The influence of the RMF on the microstructure has been studied.

(1) The RMF has a significant effect on both the thermal conditions and the microstructure only for the lower growth rate of about 0.02 mm/s, whereas it has no significant influence at the higher growth rate of 0.20 mm/s. In the case of natural convection, the impact of forced flow on the solidification process can be evaluated by comparing the velocity of the forced fluid flow to the growth rate. Indeed, the higher the ratio of the convective flow to the growth rate, the higher the impact of the convection on the microstructure. Similarly, in the experiments described here, an effect of the RMF on the microstructure characteristics is observed only for the highest ratio of the forced flow velocity to the growth rate.

(2) When the flow velocity induced by the RMF is significantly higher than the growth rate, it induces a decrease of the measured temperature gradient ahead of the liquidus isotherm and liquidus isotherm velocity, as well as a more uniform Si concentration in the liquid. Consequently, more uniform eutectic distribution without any large eutectic pockets, and lower average eutectic percentage and dendrite arm spacing are achieved.

(3) Moreover, the RMF can induce the deflection of dendrite growth direction. This phenomenon is ascribed to the combined effects of the forced liquid flow and to the thermoelectric magnetic force on the dendrites.

However, in the experiments presented in this paper, the application of a RMF could not induce the CET indicating that the forced flow was not strong enough to contribute to the dendrite fragmentation and/or to the transport of fragments outside the mushy zone. Other experiments should be conducted with a higher magnetic field intensity to confirm that CET can be triggered by the application of a forced flow, exclusively due to a RMF in μg conditions. However, the

parameters should be adjusted cautiously to avoid the formation of a large central segregated channel that appears when applying a more intense rotating magnetic field. In parallel, simulations including the TEMF forces calculations in the presence of a RMF would be useful to further study the effect of the TEMF.

Acknowledgment

This research work is supported by the European Space Agency under the CETSOL (Columnar to Equiaxed SOLidification processes) ESA MAP project, the French National Space Agency (CNES) and the German BMWi/DLR under FKZ 50WM1743. The authors acknowledge Hydro Aluminium Rolled Products GmbH for providing the alloys used in this paper. We would like to thank F. Bălțărețu, O. Budenkova and Y. Fautrelle from SIMAP/EPM Laboratory in Grenoble for numerical modelling of melt flow induced by the rotating magnetic field.

References

[1] J.A. Dantzig, M. Rappaz, Solidification, EFPL Press, 2009.

[2] D.R. Liu, N. Mangelinck-Noël, C.A. Gandin, G. Zimmermann, L. Sturz, H. Nguyen Thi, B. Billia, Structures in directionally solidified Al–7 wt.% Si alloys: Benchmark experiments under microgravity, Acta Mater., 64 (2014) 253-265.

[3] A.N. Turchin, M. Zuijderwijk, J. Pool, D.G. Eskin, L. Katgerman, Feathery grain growth during solidification under forced flow conditions, Acta Mater., 55 (2007) 3795-3801.

[4] Y. Osawa, S. Takamori, T. Kimura, K. Minagawa, H. Kakisawa, Morphology of Intermetallic Compounds in Al-Si-Fe Alloy and Its Control by Ultrasonic Vibration, Mater. Trans., 48 (2007) 2467-2475.

[5] M.C. Flemings, Behavior of metal alloys in the semisolid state, Metall. Trans. B, 22 (1991) 269-293.

[6] A.M. Holmes, X. Wang, N. Ma, D.F. Bliss, G.W. Iseler, Vertical gradient freezing using submerged heater growth with rotation and with weak magnetic and electric fields, Int. J. Heat Fluid Flow, 26 (2005) 792-800.

[7] E. Cadirli, H. Kaya, D. Rabiger, S. Eckert, M. Gunduz, Effect of rotating magnetic field on the microstructures and physical properties of Al-Cu-Co ternary eutectic alloy, J. Alloys Compd., 647 (2015) 471-480.

[8] Z. Chen, X. Wen, C. Chen, Fluid flow and microstructure formation in a rotating magnetic field during the directional solidification process, J. Alloys Compd., 491 (2010) 395-401.

[9] S. Steinbach, L. Ratke, The effect of rotating magnetic fields on the microstructure of directionally solidified Al–Si–Mg alloys, Mater. Sci. Eng., A, 413-414 (2005) 200-204.

[10] X. Li, Y. Fautrelle, Z. Ren, Influence of thermoelectric effects on the solid–liquid interface shape and cellular morphology in the mushy zone during the directional solidification of Al–Cu alloys under a magnetic field, Acta Mater., 55 (2007) 3803-3813.

[11] Z. Yan, X. Li, Z. Cao, X. Zhang, T. Li, Grain refinement of horizontal continuous casting of the CuNi10Fe1Mn alloy hollow billets by rotating magnetic field (RMF), Mater. Lett., 62 (2008) 4389-4392.

[12] A. Kao, B. Cai, P.D. Lee, K. Pericleous, The effects of Thermoelectric Magnetohydrodynamics in directional solidification under a transverse magnetic field, J. Cryst. Growth, 457 (2017) 270-274.

[13] B. Zhang, J. Cui, G. Lu, Effect of low-frequency magnetic field on macrosegregation of continuous casting aluminum alloys, Mater. Lett., 57 (2003) 1707-1711.

[14] S. Steinbach, L. Ratke, The influence of fluid flow on the microstructure of directionally solidified AlSi-base alloys, Metall. Mater. Trans. A, 38A (2007) 1388-1394.

[15] D. Samanta, N. Zabaras, Control of macrosegregation during the solidification of alloys using magnetic fields, Int. J. Heat Mass Transfer, 49 (2006) 4850-4866.

[16] H. Liu, W.D. Xuan, X.L. Xie, C.J. Li, J. Wang, J.B. Yu, X. Li, Y.B. Zhong, Z.M. Ren, Columnar-to-Equiaxed Transition and Equiaxed Grain Alignment in Directionally Solidified Ni3Al Alloy Under an Axial Magnetic Field, Metall. Mater. Trans. A, 48A (2017) 4193-4203.

[17] X.D. Wang, T.J. Li, Y. Fautrelle, M.D. Dupouy, J.Z. Jin, Two kinds of magnetic fields induced by one pair of rotating permanent magnets and their application in stirring and controlling molten metal flows, J. Cryst. Growth, 275 (2005) e1473-e1479.

[18] J.A. Shercliff, Thermoelectric magnetohydrodynamics, J. Fluid Mech., 91 (1979) 231-251.

[19] S.D. Hu, Y.C. Dai, A. Gagnoud, Y. Fautrelle, R. Moreau, Z.M. Ren, K. Deng, C.J. Li, X. Li, Effect of a magnetic field on macro segregation of the primary silicon phase in hypereutectic Al-Si alloy during directional solidification, J. Alloys Compd., 722 (2017) 108-115.

[20] M.X. Wu, T. Liu, M. Dong, J.M. Sun, S.L. Dong, Q. Wang, Directional solidification of Al-8 wt. % Fe alloy under high magnetic field gradient, J. Appl. Phys., 121 (2017).

[21] L. Abou-Khalil, J. Wang, G. Salloum-Abou-Jaoude, M. Garrido, X. Li, Z. Ren, G. Reinhart, H. Nguyen-Thi, Y. Fautrelle, Investigation of Thermo-Electro-Magnetic force on equiaxed grain motion during upward directional solidification, Int. J. Therm. Sci., 145 (2019) 106047.

[22] X. Li, Y. Fautrelle, A. Gagnoud, D. Du, J. Wang, Z. Ren, H. Nguyen-Thi, N. Mangelinck-Noel, Effect of a weak transverse magnetic field on solidification structure during directional solidification, Acta Mater., 64 (2014) 367-381.

[23] F. Bai, M. Sha, T. Li, L. Lu, Influence of rotating magnetic field on the microstructure and phase content of Ni–Al alloy, J. Alloys Compd., 509 (2011) 4835-4838.

[24] G. Zimmermann, A. Weiss, Z. Mbaya, Effect of forced melt flow on microstructure evolution in AlSi7Mg0.6 alloy during directional solidification, Mater. Sci. Eng., A, 413-414 (2005) 236-242.

[25] P.A. Davidson, An Introduction to Magnetohydrodynamics, Cambridge University Press, Cambridge, 2001.

[26] P.A. Nikrityuk, K. Eckert, R. Grundmann, A numerical study of unidirectional solidification of a binary metal alloy under influence of a rotating magnetic field, Int. J. Heat Mass Transfer, 49 (2006) 1501-1515.

[27] S. Steinbach, L. Ratke, Experimental study on interaction of fluid flow and solidification in Al-Si-Cu alloys, Int. J. Cast Met. Res., 20 (2007) 140-144.

[28] Z. Fan, G. Liu, M. Hitchcock, Solidification behaviour under intensive forced convection, Mater. Sci. Eng., A, 413-414 (2005) 229-235.

[29] H. Chen, J.C. Jie, K. Svynarenko, H.J. Ma, T.J. Li, Effect of rotating magnetic field on the fading effect of Al-5Ti-1B in commercial pure Al, J. Mater. Res., 29 (2014) 1656-1663.

[30] O. Budenkova, F. Baltaretu, J. Kovacs, A. Roosz, A. Ronafoldi, A.M. Bianchi, Y. Fautrelle, Simulation of a directional solidification of a binary Al-7wt%Si and a ternary alloy Al-7wt%Si-1wt%Fe under the action of a rotating magnetic field, in: A. Ludwig (Ed.) Mcwasp Xiii: International Conference on Modeling of Casting, Welding and Advanced Solidification Processes, 2012.

[31] M. Kissné Svéda, A. Sycheva, J. Kovács, A. Rónaföldi, A. Roósz, The effect of rotating magnetic field on the solidified structure of Sn-Cd peritectic alloys, in: Mater. Sci. Forum 2014, pp. 414-419.

[32] J.K. Roplekar, J.A. Dantzig, A study of solidification with a rotating magnetic field, Int. J. Cast Met. Res., 14 (2001) 79-95.

[33] S. Steinbach, L. Ratke, The effect of rotating magnetic fields on the microstructure of directionally solidified Al–Si–Mg alloys, Mater. Sci. Eng., A, 413-414 (2005) 200-204.

[34] B. Willers, S. Eckert, U. Michel, I. Haase, G. Zouhar, The columnar-to-equiaxed transition in Pb–Sn alloys affected by electromagnetically driven convection, Mater. Sci. Eng., A, 402 (2005) 55-65.

[35] H. Li, J.C. Jie, H. Chen, P.C. Zhang, T.M. Wang, T.J. Li, Effect of rotating magnetic field on the microstructure and properties of Cu-Ag-Zr alloy, Mater. Sci. Eng., A, 624 (2015) 140-147.

[36] M.D. Dupouy, D. Camel, Effects of gravity on columnar dendritic growth of metallic alloys: flow pattern and mass transfer, J. Cryst. Growth, 183 (1998) 469-489.

[37] G. Reinhart, C.A. Gandin, N. Mangelinck-Noel, H. Nguyen-Thi, J.E. Spinelli, J. Baruchel, B. Billia, Influence of natural convection during upward directional solidification: A comparison between in situ X-ray radiography and direct simulation of the grain structure, Acta Mater., 61 (2013) 4765-4777.

[38] M. Hainke, J. Friedrich, G. Müller, Numerical study on directional solidification of AlSi alloys with rotating magnetic fields under microgravity conditions, J. Mater. Sci., 39 (2004) 2011-2015.

[39] R. Jansen, P.R. Sahm, Solidification under microgravity, Mater. Sci. Eng., 65 (1984) 199-212.

[40] S. Akamatsu, H. Nguyen-Thi, In situ observation of solidification patterns in diffusive conditions, Acta Mater., 108 (2016) 325-346.

[41] G. Zimmermann, L. Sturz, B. Billia, N. Mangelinck-Noel, H.N. Thi, C.A. Gandin, D.J. Browne, W.U. Mirihanage, Investigation of columnar-to-equiaxed transition in solidification processing of AlSi alloys in microgravity - The CETSOL project, in: A. Meyer, I. Egry (Eds.) International Symposium on Physical Sciences in Space, 2011.

[42] G. Zimmermann, L. Sturz, H. Nguyen-Thi, N. Mangelinck-Noel, Y.Z. Li, C.-A. Gandin, R. Fleurisson, G. Guillemot, S. McFadden, R.P. Mooney, P. Voorhees, A. Roosz, A. Ronaföldi,

C. Beckermann, A. Karma, C.-H. Chen, N. Warnken, A. Saad, G.-U. Grün, M. Grohn, I. Poitrault, T. Pehl, I. Nagy, D. Todt, O. Minster, W. Sillekens, Columnar and Equiaxed Solidification of Al-7 wt.% Si Alloys in Reduced Gravity in the Framework of the CETSOL Project, JOM, 69 (2017) 1269-1279.

[43] Y.Z. Li, N. Mangelinck-Noël, G. Zimmermann, L. Sturz, H. Nguyen-Thi, Effect of solidification conditions and surface pores on the microstructure and columnar-to-equiaxed transition in solidification under microgravity, J. Alloys Compd., 749 (2018) 344-354.

[44] G. Zimmermann, Estimation of the influence of RMF on the melt flow and segregation in CETSOL2#2 Flight experiment, CETSOL project internal report, (2012).

[45] Y.H. Zhang, C.Y. Ye, Y.Y. Xu, H.G. Zhong, X.R. Chen, X.C. Miao, C.J. Song, Q.J. Zhai, Influence of Growth Velocity on the Separation of Primary Silicon in Solidified Al-Si Hypereutectic Alloy Driven by a Pulsed Electric Current, Metals, 7 (2017).

[46] Y.Z. Li, N. Mangelinck-Noël, G. Zimmermann, L. Sturz, H. Nguyen-Thi, Comparative study of directional solidification of Al-7 wt% Si alloys in Space and on Earth: Effects of gravity on dendrite growth and Columnar-to-equiaxed transition, J. Cryst. Growth, 513 (2019) 20-29.

[47] X. Li, A. Gagnoud, Y. Fautrelle, Z. Ren, R. Moreau, Y. Zhang, C. Esling, Dendrite fragmentation and columnar-to-equiaxed transition during directional solidification at lower growth speed under a strong magnetic field, Acta Mater., 60 (2012) 3321-3332.

[48] T. Enz, S. Steinbach, D. Simicic, G. Kasperovich, L. Ratke, First Experiments Using the Materials Science Laboratory on Board the International Space Station, Microgravity Sci. Technol., 23 (2011) 345-353.

[49] H. Alfvén, Existence of Electromagnetic-Hydrodynamic Waves, Nature, 150 (1942) 405.

[50] J. Wang, Y. Fautrelle, Z.M. Ren, X. Li, H. Nguyen-Thi, N. Mangelinck-Noel, G.S. Abou Jaoude, Y.B. Zhong, I. Kaldre, A. Bojarevics, L. Buligins, Thermoelectric magnetic force

1 acting on the solid during directional solidification under a static magnetic field, Appl. Phys.
2 Lett., 101 (2012) 251904.
3 [51] J. Wang, Y. Fautrelle, Z. Ren, H. Nguyen-Thi, G. Salloum Abou Jaoude, G. Reinhart, N.
4 Mangelinck-Noël, X. Li, I. Kaldre, Thermoelectric magnetic flows in melt during directional
5 solidification, Appl. Phys. Lett., 104 (2014) 121916.